


Quantum Griffiths singularity in three-dimensional MoTiN superconducting films

Zi-Xiao Wang, Tian-Yu Jing, Zi-Yan Han, Kuang-Hong Gao, Songci Li , and Zhi-Qing Li ^{*}
*Tianjin Key Laboratory of Low Dimensional Materials Physics and Preparing Technology,
 Department of Physics, Tianjin University, Tianjin 300354, China*

 (Received 2 February 2024; revised 18 April 2024; accepted 5 June 2024; published 17 June 2024)

Quantum Griffiths singularity (QGS) has been experimentally observed in a range of two-dimensional (2D) superconducting systems. Although it is theoretically suggested that the QGS also exists in three-dimensional (3D) superconductors, there is almost no experimental support to the theoretical prediction. In the present paper, we observe the occurrence of QGS in a series of ~ 80 -nm-thick $\text{Mo}_{0.8}\text{Ti}_{0.2}\text{N}_x$ ($0.84 \lesssim x \lesssim 1.12$) superconducting films (with a NaCl structure) near the field-driven superconductor-metal transition (SMT). For each film, the low-temperature magnetoresistance isotherms, measured at magnetic fields being perpendicular or parallel to the film plane, do not cross at a single point but in a wide region. The dynamical critical exponents $z\nu_{\perp}$ (for perpendicular field) and $z\nu_{\parallel}$ (for parallel field) obtained by analyzing the related magnetoresistance isotherms increase with decreasing temperature and tend to diverge as $T \rightarrow 0$ K. In addition, the corrected resistivities for the perpendicular and parallel field in the vicinity of the SMTs both obey an activated scaling based on the random transverse-field Ising model. Although these films are 3D with respect to the superconductivity, the activated scaling near the SMT for these films is as same as that for 2D superconductors with QGS. The QGS in the 3D $\text{Mo}_{0.8}\text{Ti}_{0.2}\text{N}_x$ superconducting films originates from the slow dynamics of the rare regions in these systems. We also fabricate a ~ 80 -nm-thick $(\text{Mo}_{0.8}\text{Ti}_{0.2})_2\text{N}_{1.06}$ superconducting film with face-centered cubic structure at low nitrogen partial pressure. It is found that the low-temperature magnetoresistance isotherms for the perpendicular (parallel) field cross at a single point and the resistivity data for the perpendicular (parallel) field in the vicinity of the field-induced SMT obey the power-law scaling deduced from the dirty-boson model. Our results provide unambiguous experimental evidence for the existence of QGS in 3D superconductors.

DOI: [10.1103/PhysRevB.109.224508](https://doi.org/10.1103/PhysRevB.109.224508)

I. INTRODUCTION

Quantum Griffiths singularity (QGS) has been discovered in a range of two-dimensional (2D) superconducting systems and attracted great attention over the past decade [1–4]. Conceptually, the QGS refers to the phenomenon that certain thermodynamic observables of a system are singular not just at criticality but in a finite region in the vicinity of the quantum critical point. As for the 2D superconducting systems, the main characteristic of QGS is that the low-temperature magnetoresistance isotherms do not cross at a point near the critical field but at multiple points, and the dynamical critical exponent $z\nu$ obtained at each crossing point diverges as $T \rightarrow 0$ K [1–4]. Experimentally, the existence of QGS was initially reported in three-dimensional (3D) magnetic materials, including 3D heavy fermion systems and f -electron ferromagnetic alloys [5–8]. Until 2015, the QGS was observed in three-monolayer Ga films, providing experimental evidence for the presence of QGS in 2D superconducting system [1]. Thereafter, QGS was observed in many 2D superconducting systems, such as $\text{LaAlO}_3/\text{SrTiO}_3$ interface [2], monolayer NbSe_2 films [3], ion-gated ZrNCl and MoS_2 [4]. More recently, the existence of QGS has also been confirmed in 2D InO_x [9], WSi [10], β -W [11], Li_xMoS_2 [12], and

NbN films [13,14]. In addition, it has been reported that in four-monolayer crystalline PdTe_2 films the QGS can emerge not only in perpendicular fields but also in parallel magnetic fields [15]. According to previous reports [1–4], quenched disorder is the main origin of the QGS. On the other hand, the theoretical results indicate that the QGS can occur in both 2D and 3D systems [16–22], and the QGS has been observed in 3D magnetic materials [5–8]. However, there is almost no experimental evidence for the existence of QGS in 3D superconducting system thus far [23,24]. Therefore, it is desirable to explore whether there is QGS in 3D superconductors.

MoN-based films with NaCl structure could be a suitable system to realize the QGS in 3D superconducting films. In 1980s, it was predicted that the superconducting transition temperature T_c of MoN with NaCl structure (so called $B1$ -MoN) could be as high as 29 K [25,26]. However, the predicted high transition temperature has not yet been achieved in $B1$ -MoN probably due to its structural instability (the existence of many Mo or nitrogen vacancies, dislocations and other defects) [27–32]. In addition, it has been found that adding Ti to $B1$ -MoN can stabilize its structure [33]. Therefore, to explore whether the T_c of Ti stabilized $B1$ -MoN is enhanced, we fabricated a series of $B1$ - $\text{Mo}_{0.8}\text{Ti}_{0.2}\text{N}_x$ films with different nitrogen contents x . Although the superconducting transition temperature of the MoTiN films were not significantly improved as expected, it is found that 3D MoTiN films possess relatively high T_c and low upper critical

^{*}Contact author: zhiqingli@tju.edu.cn

magnetic field (see in the following text). These features, together with the nature of easily formed structural defects, could make MoTiN films be a suited system for exploring the characteristics of 3D QGS. In the present paper, the low-temperature electrical transport properties of a series of ~ 80 -nm-thick $\text{Mo}_{0.8}\text{Ti}_{0.2}\text{N}_x$ films with x ranging from ~ 0.53 to ~ 1.36 were studied. The QGS is found emerging in the $0.84 \lesssim x \lesssim 1.12$ films. We present and discuss the interesting observations in the following sections.

II. EXPERIMENTAL METHOD

Our MoTiN films with thickness $t \sim 80$ nm were grown on (100) MgO single crystal substrates by the reactive magnetron sputtering method. A MoTi alloy target with Mo/Ti ratio of 8 : 2 and purity of 99.9% was selected as the sputtering source. The base pressure of the chamber was less than 1×10^{-4} Pa. During the deposition, the sputtering power was set as 300 W, and the substrate temperature and sputtering pressure were kept at 500°C and 0.15 Pa, respectively. The deposition was carried out in a mixture of argon (99.999%) and nitrogen (99.999%) atmosphere. To obtain MoTiN films with different superconducting transition temperatures, the volume ratio of nitrogen to argon was controlled in each deposition round. For the films used in this paper, the volume ratios were set as 1 : 9, 1 : 7, 3 : 17, 7 : 33, 1 : 4, and 1 : 3 (corresponding to nitrogen partial pressures $P_{\text{N}_2} \simeq 10.0\%$, 12.5%, 15.0%, 17.5%, 20.0%, and 25.0%), respectively.

The thicknesses of the film was controlled by growth rate and deposition time, and further determined by the high-resolution transmission electron microscopy (HRTEM) of the cross section of the film. The crystal structure was determined by x-ray diffraction (XRD), including normal θ - 2θ , ϕ , and ω scans. The composition of the film and valence of each element were measured using a x-ray photoelectron spectrometer (Thermo Scientific Escalab 250Xi). Before the x-ray photoelectron spectroscopy (XPS) measurement was carried out, the surface of each film was etched by Ar ions and the corrosion depth was ~ 20 nm. The microstructure of the films was characterized by transmission electron microscopy (TEM, Tecnai G2 F20 S-Twin). The longitudinal and Hall resistance vs temperature and magnetic field was measured using the standard four-probe method in a physical properties measurement system (PPMS-6000, Quantum Design) equipped with a ^3He refrigerator. Hall-bar-shaped films (1.0-mm wide, 10.0-mm long, and 3.0-mm distance between the two electrodes) defined by mechanical masks were used in the measurements. For the longitudinal resistance vs magnetic field at a fixed temperature and longitudinal resistance vs temperature at a fixed field measurements, the field was applied in directions being perpendicular and parallel to the film plane, respectively. In the latter case, the field was also perpendicular to the excitation current.

III. RESULTS AND DISCUSSIONS

The XRD and HRTEM results indicate that all the MoTiN films have a face-centered cubic (fcc) structure and are epitaxially grown on the (100) MgO single-crystal substrates. For the film deposited at $P_{\text{N}_2} \simeq 10.0\%$, the nominal composition can be expressed as $(\text{Mo}_{0.8}\text{Ti}_{0.2})_2\text{N}_{1.06}$, the lattice constant

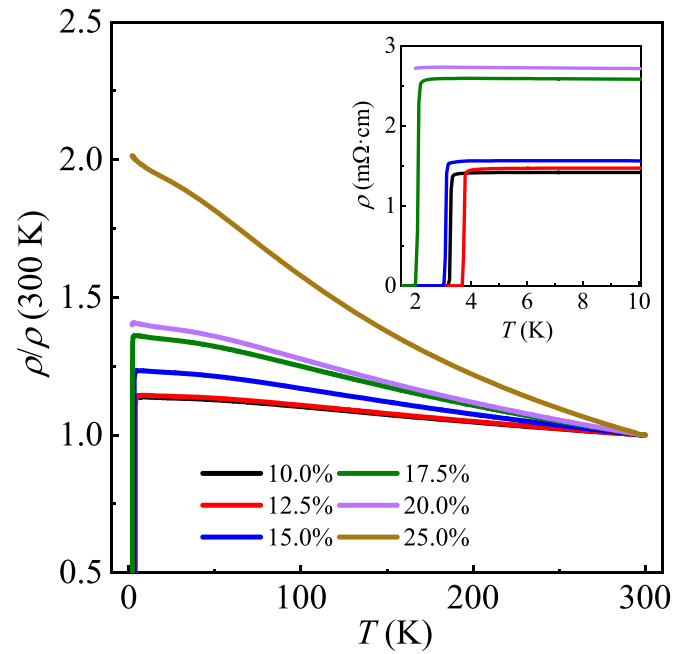


FIG. 1. Normalized resistivity as a function of temperature for the MoTiN films deposited at different nitrogen partial pressures. Inset: Resistivity vs temperature at low-temperature regime for films deposited at $P_{\text{N}_2} \lesssim 20.0\%$.

a (4.191 \AA) and the XPS spectra of Mo and N atoms are comparable to those for γ - Mo_2N . These suggest that the film is crystallized into a phase similar to that of γ - Mo_2N . For the films deposited at $12.5\% \lesssim P_{\text{N}_2} \lesssim 25.0\%$, the nominal compositions can be written as $\text{Mo}_{0.8}\text{Ti}_{0.2}\text{N}_x$, and the lattice constants and XPS spectra of Mo and N atoms are close to those of the fcc-MoN compound, implying that $\text{Mo}_{0.8}\text{Ti}_{0.2}\text{N}_x$ films with $B1$ structure are formed under these N_2 partial pressures. The x value and lattice constant for each film are listed in Table I. The detailed analyses concerning the structures, atomic valences, and compositions of the MoTiN films are given in the Appendix. In the following subsections, we will first explore the fundamental transport properties of the films. Then we will study the characteristics of the quantum phase transition driven by magnetic field. For clarity, we use \perp (\parallel) as the superscript or subscript of a physical quantity to represent that the quantity is related to the field perpendicular (parallel) to the film plane.

A. Fundamental transport properties

Figure 1 shows the normalized resistivity $\rho/\rho(300 \text{ K})$ as a function of temperature T for the films deposited at different nitrogen partial pressures. The resistivities of all the films slightly increase with decreasing temperature above liquid helium temperature, i.e., the temperature coefficient of the resistivity $(1/\rho)(d\rho/dT)$ for each film is negative at high-temperature regime. The films deposited at $P_{\text{N}_2} \lesssim 17.5\%$ enter into superconducting state below the superconducting transition temperature T_c , where T_c is designated as the temperature at which the resistance drops to 90% of that in normal state [$\rho(10 \text{ K})$, see the inset of Fig. 1]. For the $B1$ - $\text{Mo}_{0.8}\text{Ti}_{0.2}\text{N}_x$ films, the superconducting transition temperature increases

TABLE I. Relevant parameters of the $\text{Mo}_{0.8}\text{Ti}_{0.2}\text{N}_x$ films. Here a is the lattice constant, FWHM is the full width at half maximum in the rocking curve, $\rho(300\text{ K})$ is the resistivity at 300 K, T_c is the superconducting transition temperature, $n(10\text{ K})$ is the carrier concentration at 10 K, $k_F\ell$ is the Ioffe-Regel parameter at 10 K, $B_{c2}^{\perp}(0)$ is the upper critical magnetic field at 0 K, and ξ_{GL} is the Ginzburg-Landau coherence length. The superscripts \perp and \parallel represent the related quantities obtained for perpendicular and parallel field, respectively.

Film No.	P_{N_2} (%)	a (Å)	FWHM (degree)	x	$\rho(300\text{ K})$ ($\text{m}\Omega\text{ cm}$)	T_c (K)	$n(10\text{ K})$ (10^{23} cm^{-3})	$k_F\ell$	$B_{c2}^{\perp}(0)$ (T)	$B_{c2}^{\parallel}(0)$ (T)	ξ_{GL}^{\perp} (nm)	$\xi_{\text{GL}}^{\parallel}$ (nm)
1	10.0	4.191	0.064	0.53	1.245	3.30	2.53	2.78	5.21	7.38	7.96	6.68
2	12.5	4.228	0.046	0.84	1.267	3.75	2.47	2.69	6.05	8.21	7.38	6.34
3	15.0	4.232	0.115	1.05	1.284	3.13	2.41	2.55	5.23	7.27	7.94	6.73
4	17.5	4.255	0.045	1.12	1.904	2.15	2.03	1.63	3.49	5.73	9.72	7.59
5	20.0	4.257	0.043	1.20	1.942		1.97	1.56				
6	25.0	4.272	0.049	1.36	2.902		1.85	0.76				

with decreasing nitrogen partial pressure, while the T_c of the $P_{\text{N}_2} \simeq 10.0\%$ [$\gamma\text{-}(\text{Mo}_{0.8}\text{Ti}_{0.2})_2\text{N}_{1.06}$] film is less than that of the $P_{\text{N}_2} \simeq 12.5\%$ [$\text{B1-Mo}_{0.8}\text{Ti}_{0.2}\text{N}_{0.84}$] film. Using free-electron model, one can obtain the product of the Fermi wave number and mean free path of electrons $k_F\ell$ via $k_F\ell = (\hbar/e^2)(3\pi^2)^{1/3}n^{-2/3}/\rho$, where \hbar is the Planck's constant divided by 2π , e is the electronic charge, and n is the carrier concentration. The values of $k_F\ell$ for the films at 10 K are summarized in Table I. Inspection of Table I indicates that the $k_F\ell$ is 0.76 for the $P_{\text{N}_2} \simeq 25.0\%$ film, and varies between 1.56 and 2.78 for other films. According to the Ioffe-Regel criterion [34], the $P_{\text{N}_2} \simeq 25.0\%$ film just lies in the metal-insulator transition region, while the other films are on the metal side of the metal-insulator transition and in a bad metallic state.

Figures 2(a) and 2(b) show the temperature dependence of the perpendicular and parallel upper critical fields for the $P_{\text{N}_2} \lesssim 17.5\%$ films. The experimental $B_{c2}^{\perp}\text{-}T$ and $B_{c2}^{\parallel}\text{-}T$ data are fitted to $B_{c2}^i(T) = B_{c2}^i(0)[1 - (T/T_c)^2]$ [35], where $i = \perp$ and \parallel stand for the perpendicular-field and parallel-field situations, respectively, and $B_{c2}^i(0)$ is the upper critical magnetic field at 0 K. The fitted results are shown in Fig. 2 by the dashed curves. The values of the adjusting parameters $B_{c2}^{\perp}(0)$ and $B_{c2}^{\parallel}(0)$ are obtained and listed in Table I. Inspection of Table I indicates that $B_{c2}^{\parallel}(0)$ is only slightly greater than $B_{c2}^{\perp}(0)$ for each film, suggesting the films are

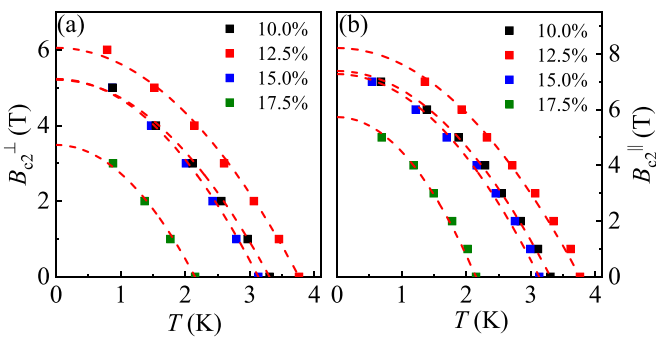


FIG. 2. (a) The perpendicular upper critical magnetic field B_{c2}^{\perp} vs temperature T for the films deposited at $P_{\text{N}_2} \lesssim 17.5\%$. (b) The parallel upper critical magnetic field B_{c2}^{\parallel} vs temperature T for the films deposited at $P_{\text{N}_2} \lesssim 17.5\%$. The dashed curves are the least-squares fits to $B_{c2}^i(T) = B_{c2}^i(0)[1 - (T/T_c)^2]$ with $i = \perp$ in (a) and $i = \parallel$ in (b).

3D with respect to superconductivity. Once the values of $B_{c2}^{\perp}(0)$ and $B_{c2}^{\parallel}(0)$ are obtained, one can deduce the Ginzburg-Landau (GL) coherence lengths ξ_{GL}^{\perp} and $\xi_{\text{GL}}^{\parallel}$ for each film via $\xi_{\text{GL}}^i = [\Phi_0/(2\pi B_{c2}^i(0))]^{1/2}$ [35], where $\Phi_0 = h/2e$ is the flux quantum. The GL coherence lengths ξ_{GL}^{\perp} and $\xi_{\text{GL}}^{\parallel}$ for each superconducting film are also listed in Table I. Clearly, the coherence length perpendicular to the film plane ξ_{GL}^{\perp} lies between ~ 7 and ~ 10 nm, while the coherence length parallel to the film plane $\xi_{\text{GL}}^{\parallel}$ varies between ~ 6 and ~ 8 nm. For each film, ξ_{GL}^{\perp} is comparable with $\xi_{\text{GL}}^{\parallel}$ and much less than the thickness of the film, which further confirms the 3D superconductive characteristics of the MoTiN films.

B. Quantum phase transition

In this subsection, we will focus on the quantum phase transitions in these 3D superconducting films deposited at $P_{\text{N}_2} \lesssim 17.5\%$. We first explore the temperature-dependent behavior of the resistivity evolution with external field. Figure 3(a) shows the resistivity variation with temperature from 5.00 down to 0.50 K under different perpendicular fields for a representative film deposited at $P_{\text{N}_2} \simeq 15.0\%$. Figure 3(b) is the close view of the superconducting transition region. When the field is less than ~ 6 T, the film transforms from normal state to superconducting state upon cooling and the superconducting transition temperature decreases with increasing field. As the magnetic field is increased to 7 T, the resistivity slightly increases with decreasing temperature over the whole measured temperature range. Considering the $k_F\ell$ of the film is 2.55 at 10 K, one can deduce that the film transforms into a bad metallic state under 7 T. Inspection of Fig. 3(b) also indicates that the critical field for superconductor-metal transition (SMT) is in the vicinity of ~ 6.0 T. Figure 3(c) shows the resistivity vs temperature at different parallel fields for the same film. Similar to the situation at perpendicular field, the parallel field also drives the film from a superconducting state to a bad metallic state. The parallel critical field for SMT lies in the vicinity of ~ 8.0 T [see Fig. 3(d)], being slightly larger than the perpendicular critical field. In Figs. S4 and S5 within the Supplemental Material [36], we give the resistivity vs temperature measured at different perpendicular fields and parallel fields, respectively, for the $P_{\text{N}_2} \simeq 17.5\%$, 12.5%, and 10.0% films. The temperature-dependent behaviors of the resistivity evolution with external fields for these

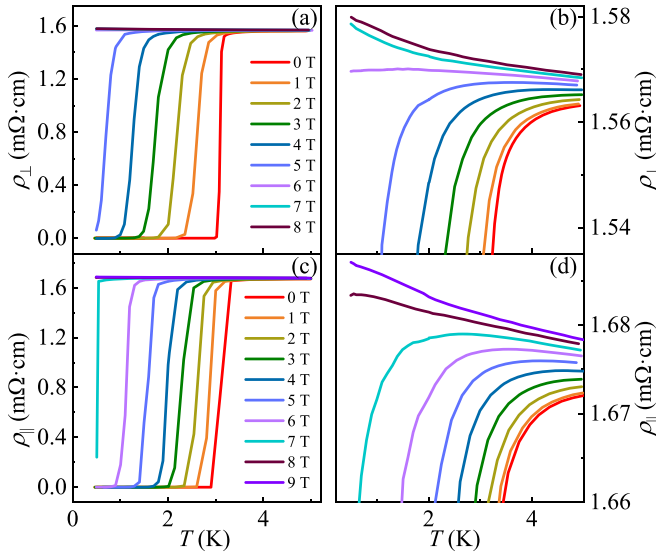


FIG. 3. (a) The resistivity as a function of temperature in different fields (perpendicular to the film plane) for the film deposited at $P_{N_2} \simeq 15.0\%$. (b) The resistivity as a function of temperature in different fields (parallel to the film plane) for the film deposited at $P_{N_2} \simeq 15.0\%$. (c) and (d) are the enlarged views of the corresponding films near the superconducting transition region.

films are similar to those for the $P_{N_2} \simeq 15.0\%$ film. Checking Fig. 3, and Figs. S4, and S5 within the Supplemental Material [36], one can conclude that all the films will transform from a superconducting state to a bad metallic state by applying a perpendicular or parallel field with sufficient magnitude, and the film with higher zero field superconducting transition temperature possesses higher perpendicular and parallel critical fields for SMT.

For field-induced SMT or superconductor-insulator transition (SIT), the dirty-boson model predicts that the field dependence of resistance curves at different temperatures all cross at a single point with $B = B_c$ (B_c is the critical field) [37–39]. In addition, near the SMT (SIT) the resistance at different fields and temperatures obeys a power-law scaling form [40,41]

$$R(B, T) = R_c f(\delta T^{-1/z\nu}), \quad (1)$$

where R_c is the critical resistance, $f(x)$ is the scaling function with $f(0) = 1$, $\delta = |B - B_c|$ is the distance from the critical field B_c , ν is the correlation length exponent, z is the dynamical critical exponent. For the scaling predicated by Eq. (1), the spatial correlation length ξ and temporal correlation length ξ_τ diverge as $\xi \sim |\delta|^{-\nu}$ and $\xi_\tau \sim \xi^z \sim |\delta|^{-z\nu}$, in the vicinity of the SMT (SIT). At finite temperatures, maximum possible value of ξ_τ is $\hbar/k_B T$ with \hbar being the Planck constant and k_B being Boltzmann constant, and thus has finite value. The theory accounting for finite size in temporal direction is called finite size scaling [42–46]. Experimentally, the power-law scaling in Eq. (1) has been observed in a range of 2D superconductors near the SIT or SMT. The values of $z\nu$ were generally found to be ≈ 0.65 [47], ≈ 1.33 [37,48], and ≈ 2.33 [38,39], which correspond to the universality class of $(2+1)DXY$ model [45], classic percolation model [38], and

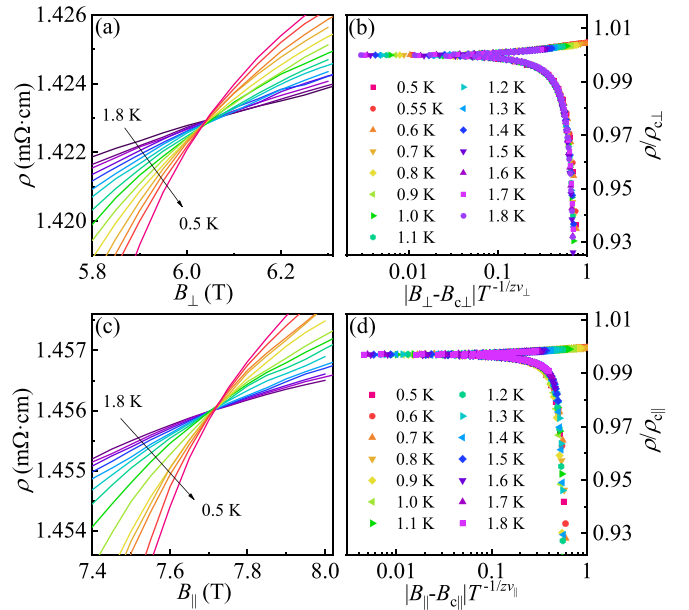


FIG. 4. (a) Resistivity vs perpendicular field at different temperatures ranging from 0.50 to 1.80 K for the $P_{N_2} \simeq 10.0\%$ film. (b) Normalized resistivity $\rho/\rho_{c\perp}$ as a function of the scaling variable $|B_{\perp} - B_{c\perp}|T^{-1/z\nu_{\perp}}$ measured at perpendicular field. (c) Resistivity versus parallel field at different temperatures ranging from 0.50 to 1.80 K for the $P_{N_2} \simeq 10.0\%$ film. (d) Normalized resistivity $\rho/\rho_{c\parallel}$ as a function of the scaling variable $|B_{\parallel} - B_{c\parallel}|T^{-1/z\nu_{\parallel}}$ measured at parallel field.

quantum percolation model [38], respectively. As mentioned in Sec. I, in some 2D superconducting films, the magnetoresistance isotherms do not intersect at a single point or narrow region, but rather in a wide region, indicating the presence of QGS accompanying the SMT.

To explore whether the QGS could occur in 3D superconductors, we measured the magnetoresistance isotherms of the $(\text{Mo}_{0.8}\text{Ti}_{0.2})\text{N}_{1.06}$ film (i.e., the film deposited at $P_{N_2} \simeq 10.0\%$) measured at fields perpendicular to the film plane. Clearly, the ρ - B_{\perp} curves measured at different temperatures almost cross at a single point. The field and resistivity corresponding to the crossing point are $B_{c\perp} \approx 6.04$ T and $\rho_{c\perp} \approx 1.423$ m Ω cm. Using the values of the $\rho_{c\perp}$ and $B_{c\perp}$, we compare the $\rho(B_{\perp}, T)/\rho_{c\perp}$ data with Eq. (1). As shown in Fig. 4(b), the $\rho/\rho_{c\perp}$ vs $|B_{\perp} - B_{c\perp}|T^{-1/z\nu_{\perp}}$ collapse onto a single curve (two branches) as $z\nu_{\perp}$ is taken the appropriate value. The optimized value of $z\nu_{\perp}$ for the best collapse is $z\nu_{\perp} = 0.84 \pm 0.05$ using a numerical minimization procedure. For the parallel field case, the low-temperature magnetoresistance isotherms and related scaling curve are shown in Figs. 4(c) and 4(d), respectively. Clearly, the results are similar to those measured at the perpendicular field: the low-temperature magnetoresistance isotherms cross at a single point and the $\rho(B_{\parallel}, T)/\rho_{c\parallel}$ data obey the power-law scaling form of Eq. (1). Here the optimized scaling parameter $z\nu_{\parallel}$ is $z\nu_{\parallel} = 0.74 \pm 0.02$, and the critical resistivity and field are $\rho_{c\parallel} \approx 1.456$ m Ω cm and $B_{c\parallel} \approx 7.72$ T, respectively. It should be noted that value of $B_{c\parallel}$ is only 1.28 times as large as that

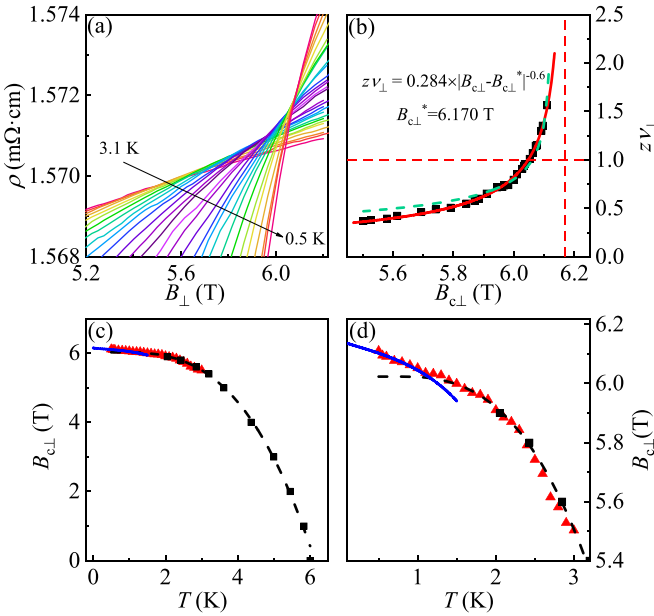


FIG. 5. (a) Resistivity vs perpendicular field at different temperatures ranging from 0.50 to 3.10 K for the film deposited at $P_{\text{N}_2} \simeq 15.0\%$. (b) $B_{c\perp}$ dependence of critical exponent $z_{\nu_{\perp}}$. The dashed vertical and horizontal lines represent the trajectories of $B_{c\perp} = B_{c\perp}^*$ and $z_{\nu_{\perp}} = 1$, respectively. (c) Temperature dependence of perpendicular critical field (solid triangles) and T_c^{on} at different fields (solid squares). The solid curve is the least-square fit to Eq. (6) and the dashed curve is only the guide to eyes. (d) The close view of the low temperature and high field region of (c).

of $B_{c\perp}$, which also supports that the $(\text{Mo}_{0.8}\text{Ti}_{0.2})_2\text{N}_{1.06}$ film is 3D with respect to superconductivity. The features of the magnetoresistance isotherms strongly suggest that the Cooper pairs in the 3D $(\text{Mo}_{0.8}\text{Ti}_{0.2})_2\text{N}_{1.06}$ film can also be described by a two-dimensional boson system and the SMT in the film is caused by quantum fluctuations. In fact, it is found that the $R(B, T)$ data of the 50-nm-thick $\text{Nb}_{0.15}\text{Si}_{0.85}$ superconducting films [47] and 3D $\text{BaPb}_{1-x}\text{Bi}_x\text{O}_3$ ($0.24 \leq x \leq 0.29$) superconductors [49] in the vicinity of the SIT can also be described by Eq. (1).

For the films deposited at $P_{\text{N}_2} \simeq 12.5\%$, 15.0% , 17.5% , the features of the low-temperature magnetoresistance isotherms are quite different from those of the $(\text{Mo}_{0.8}\text{Ti}_{0.2})_2\text{N}_{1.06}$ film. Considering the results for the three films are similar, hence, we only give and discuss the results taken from the $P_{\text{N}_2} \simeq 15.0\%$ film here. The results for the two other films are given within the Supplemental Material [36]. We first explore what happens when the field is perpendicular to the film plane. Figure 5(a) shows ρ as a function of B_{\perp} at different temperatures from 0.50 to 3.10 K. Clearly, the magnetoresistance isotherms at low temperatures do not cross at a single point or a narrow region, but cross at many points located in a relatively large transition area. These crossing points form a continuous boundary line of SMT. This phenomenon is very similar to that in 2D superconductors with QGS [1–4], and treated as a signature of QGS in 2D superconductors. We analyze the magnetoresistance isotherms in a fashion similar to those in 2D superconducting films with QGS. Assuming that ρ - B_{\perp} curves at three adjacent temperatures cross at one

point, we compare the ρ - B_{\perp} data measured at three adjacent temperatures with the transformed Eq. (1), $\rho(B, t) = \rho_c f(\delta t)$ with t being $t = (T/T_0)^{-1/z_{\nu}}$ and T_0 being the lowest temperature in each group of ρ - B_{\perp} data. Selecting the proper value of $z_{\nu_{\perp}}$, the ρ - B_{\perp} data at the three adjacent temperatures will be scaled onto two branches. Thus, the critical exponent $z_{\nu_{\perp}}$ as a function of $B_{c\perp}$, shown in Fig. 5(b), was obtained. In the high-temperature regime ($T \gtrsim 1.20$ K), $z_{\nu_{\perp}}$ increases slowly with increasing $B_{c\perp}$, while in the low-temperature regime ($T \lesssim 1.20$ K), $z_{\nu_{\perp}}$ increases rapidly and tends to diverge as $B_{c\perp} \rightarrow B_{c\perp}^*$, where $B_{c\perp}^*$ is the characteristic field. The $z_{\nu_{\perp}}$ vs $B_{c\perp}$ data are compared with the equation [20]

$$z_{\nu} = C|B_c - B_c^*|^{-\nu\psi}, \quad (2)$$

where C is a constant, ν is the correlation length exponent, and ψ is the tunneling exponent [18,19]. As mentioned in Sec. I, there are few experimental evidences concerning the occurrence of QGS in 3D superconductors. The only report we can find on QGS in 3D superconducting systems is a preprint recently announced on arXiv by Qi *et al.* [24]. In the preprint, Qi *et al.* declare that they have observed the QGS in a 3D spinel oxide MgTi_2O_4 near the superconductor to insulator transition. For the 3D spinel oxide MgTi_2O_4 , it is found that critical exponent z_{ν} vs B_c satisfy Eq. (2), and the value of $\nu\psi$ is $\nu\psi = 0.33$. Since the tunneling exponent ψ is predicted to be $1/2$, and independent of the dimensionality, the correlation length exponents for 1D, 2D, and 3D QGS are estimated to be 2, 1.2, and $2/3$, respectively according to the Harris criterion [50]. We first fit the $z_{\nu_{\perp}}$ vs $B_{c\perp}$ data of the $P_{\text{N}_2} \simeq 15.0\%$ film to Eq. (2) by setting $\nu\psi = 0.33$, and the fitting result is shown in Fig. 5(b) by the dashed curve. Inspection of the figure indicates that the theoretical prediction of Eq. (2) deviates the experimental data. We then fit the $z_{\nu_{\perp}}$ vs $B_{c\perp}$ data by taking $\nu\psi$ as 0.60. The result is presented in Fig. 5(b) by the solid curve. Clearly, the $z_{\nu_{\perp}}$ vs $B_{c\perp}$ data of the $P_{\text{N}_2} \simeq 15.0\%$ film satisfy the activated scaling described by Eq. (2), in which the fitted value of $B_{c\perp}^*$ is 6.170 T. The results for the $P_{\text{N}_2} \simeq 12.5\%$ and $P_{\text{N}_2} \simeq 17.5\%$ films are given in Figs. S5(b) and S5(e), respectively, within the Supplemental Material [36]. The values of $B_{c\perp}^*$ for the two films are listed in Table II. Although the $P_{\text{N}_2} \simeq 12.5\%$, 15.0% , 17.5% films are 3D superconductors, the correlation length exponents of the films are $\nu \simeq 2/3$, i.e., the critical exponent z_{ν} vs critical field B_c in these 3D superconducting films obey the activated scaling for 2D superconductors in the vicinity of the quantum phase transition. In actuality, the fact that the superconductivity is 3D does not necessarily mean that the physical quantities for describing the quantum phase transition obey the scaling theoretically predicted for the majority of 3D systems. For the quantum transition in a 3D superconductor, the correlation length will be greater than the thickness of the film at some temperature, which could lead to some behaviors of the superconductor in the vicinity of the transition similar to those of a 2D superconductor.

Figure 5(c) shows the temperature dependence of perpendicular critical magnetic field for the $P_{\text{N}_2} \simeq 15.0\%$ film. Here the solid triangles represent the critical field $B_{c\perp}(T)$ at each crossing point of two adjacent magnetoresistance isotherms, and the solid squares are the superconducting onset temperature $T_c^{\text{on}}(B_{\perp})$ obtained from the ρ - T curves (the temperature

TABLE II. Relevant parameters of the $\text{Mo}_{0.8}\text{Ti}_{0.2}\text{N}_x$ films deposited at $P_{\text{N}_2} \simeq 12.5\%$, 15.0% , 17.5% . Here C and B_c^* are the parameters in Eq. (2); \tilde{B}_c^* , \tilde{T}_0 , u , and y are the characteristic field, characteristic temperature, and parameters in Eq. (6). The subscripts \perp and \parallel represent the related quantities obtained for perpendicular and parallel field, respectively.

Film No.	P_{N_2} (%)	C_{\perp}	$B_{c\perp}^*$ (T)	$\tilde{B}_{c\perp}^*$ (T)	$\tilde{T}_{0\perp}$ (K)	u_{\perp}	y_{\perp}	C_{\parallel}	$B_{c\parallel}^*$ (T)	$\tilde{B}_{c\parallel}^*$ (T)	$\tilde{T}_{0\parallel}$ (K)	u_{\parallel}	y_{\parallel}
2	12.5	0.318	7.341	7.469	5.240	0.084	0.02	0.379	9.046	9.279	4.725	0.096	0.03
3	15.0	0.284	6.170	6.155	4.846	0.0256	0.008	0.434	7.962	8.075	3.314	0.063	0.012
4	17.5	0.291	4.595	4.682	2.703	0.064	0.16	0.482	6.287	6.499	3.606	0.205	0.24

for $d\rho/dT = 0$ near the superconducting transition). It should be noted that the $T_c^{\text{on}}(B_{\perp})$ data and the $B_{c\perp}(T)$ data almost follow the same trajectory above ~ 1.10 K [see the dashed line in Fig. 5(c)], which is also similar to that for 2D superconductors with QGS [1–4]. The value of $B_{c\perp}(T)$ gradually increases with decreasing temperature from 3.10 to ~ 1.10 K, and then rapidly increases with further decreasing temperature [see Fig. 5(d)], i.e., the $B_{c\perp}$ vs T data deviates from its original trajectory below ~ 1.10 K. In 2D superconductors with QGS, the temperature dependence of B_c in lower-temperature regime also deviates from its higher temperature trajectory, which is considered as another signature for the occurrence of QGS [1]. The similarities of the low-temperature magnetoresistance isotherms and the temperature-dependent behavior of B_c between the 3D $\text{Mo}_{0.8}\text{Ti}_{0.2}\text{N}_x$ superconducting films and 2D superconductors with QGS, together with the fact that the $z\nu_{\perp}$ vs $B_{c\perp}$ of the $\text{Mo}_{0.8}\text{Ti}_{0.2}\text{N}_x$ films obey the activated scaling law, strongly suggest the occurrence of QGS in the 3D $\text{Mo}_{0.8}\text{Ti}_{0.2}\text{N}_x$ films.

Figure 6(a) shows the magnetoresistance isotherms measured at fields being parallel to the film plane for the $P_{\text{N}_2} \simeq 15.0\%$ film. Similar to those in the perpendicular fields, the low-temperature ρ - B_{\parallel} curves at different temperatures do not cross at a single point or a narrow region, but at a wide range in which the field spans from ~ 6.7 to ~ 7.9 T as the temperature decreases from 3.10 to 0.50 K. The features of the magnetoresistance isotherms strongly suggest that the QGS may occur in the film as subjected to a parallel field. To verify the speculation, we analyze the magnetoresistance isotherms measured at parallel field, just like analyzing that for the perpendicular field mentioned above. Then, $z\nu_{\parallel}$ as a

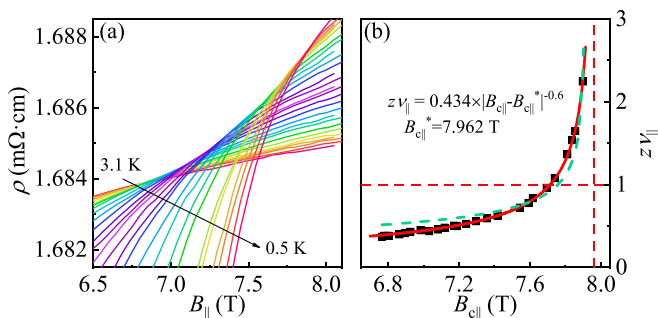


FIG. 6. (a) The resistivity vs the parallel field at different temperatures from 0.50 to 3.10 K for the $P_{\text{N}_2} \simeq 15.0\%$ film. (b) $B_{c\parallel}$ dependence of critical exponent $z\nu_{\parallel}$ for the $P_{\text{N}_2} \simeq 15.0\%$ film. The dashed vertical and horizontal lines stand for the trajectories of $B_{c\parallel} = B_{c\parallel}^*$ and $z\nu_{\parallel} = 1$, respectively.

function of the critical field $B_{c\parallel}$ is obtained, and shown in Fig. 6(b). From Fig. 6(b), one can see that the variation of $z\nu_{\parallel}$ with $B_{c\parallel}$ is quite similar to that for $z\nu_{\perp}$ with $B_{c\perp}$, i.e., the $z\nu_{\parallel}$ increases with increasing $B_{c\parallel}$ (or decreasing temperature), and tends to diverge as $T \rightarrow 0$ K. The solid curve in Fig. 6(b) is the theoretical prediction of Eq. (2), where $\nu\psi$ is set as 0.60 and the optimized parameters C_{\parallel} and $B_{c\parallel}^*$ are 0.434 and 7.962 T, respectively. Inspection of Fig. 6(b) indicates that the $z\nu_{\parallel}$ vs $B_{c\parallel}$ data can also be well described by Eq. (2) with $\nu\psi = 0.60$, just like the situation in perpendicular fields mentioned above. However, the theoretical prediction of Eq. (1) will deviate from $z\nu_{\parallel}$ vs $B_{c\parallel}$ data if we set $\nu\psi$ as 0.33, indicated as the dashed curve in Fig. 6(b). The results of the $P_{\text{N}_2} \simeq 12.5\%$ and 17.5% films are similar to that for the $P_{\text{N}_2} \simeq 15.0\%$ {see Figs. S6(b) and S6(e) within the Supplemental Material [36]}. Thus, our results suggest that both the perpendicular and parallel fields can drive the $12.5\% \lesssim P_{\text{N}_2} \lesssim 17.5\%$ films into a QGS state before entering into a bad metallic state. The critical exponents $z\nu_{\perp}$ and $z\nu_{\parallel}$ both diverge in the way of a 2D superconductor as the quantum phase transition is approached, i.e., $B_{c\perp} \rightarrow B_{c\perp}^*$ and $B_{c\parallel} \rightarrow B_{c\parallel}^*$ as $T \rightarrow 0$.

For the QGS, the critical point is infinite-randomness type with activated scaling. Based on the random transverse field Ising model, Maestro *et al.* [21] have proposed an activated scaling to describe the conductivity of nanowires near the SMT. They also suggested that the scaling should be also applicable to high-dimensional systems by taking different exponents. Recently, it has been demonstrated that the activated scaling can describe the variation of the resistance with the field and temperature near the SMT for the 2D superconductors with QGS [9,51]. According to Maestro *et al.* [21] and Lewellyn *et al.* [9], the activated dynamics scaling can be written as

$$R\left(\tilde{\delta}, \ln \frac{\tilde{T}_0}{T}\right) = \Phi\left[\tilde{\delta}\left(\ln \frac{\tilde{T}_0}{T}\right)^{1/\nu\psi}\right], \quad (3)$$

where $\tilde{\delta} = |B - \tilde{B}_c^*|/\tilde{B}_c^*$ is the relative distance from the critical field, \tilde{B}_c^* is the critical field for $T \rightarrow 0$ [52], ν is the correlation length exponent, ψ is the tunneling exponent, and \tilde{T}_0 is a microscopic temperature scale associated with the quantum phase transition. In Eq. (3), the influence of temperature was not considered. Thus, the corrections to the scaling, which result in the smeared crossing points of isotherms, should be included at finite temperatures. Recently, the inverse disorder strength is treated as an irrelevant scaling variable near the infinite-randomness critical point, and the corrected

scaling then can be expressed as [9,51]

$$R\left(\tilde{\delta}, \ln \frac{\tilde{T}_0}{T}, u\right) = \Phi\left[\tilde{\delta}\left(\ln \frac{\tilde{T}_0}{T}\right)^{\frac{1}{\nu\psi}}, u\left(\ln \frac{\tilde{T}_0}{T}\right)^{-y}\right], \quad (4)$$

where u is the leading irrelevant scaling variable, and $y > 0$ is the associated irrelevant exponent. Expanding the above scaling function in the second argument, one obtain

$$R\left(\tilde{\delta}, \ln \frac{\tilde{T}_0}{T}, u\right) \approx \Phi_1\left[\tilde{\delta}\left(\ln \frac{\tilde{T}_0}{T}\right)^{\frac{1}{\nu\psi}}\right] + u\left(\ln \frac{\tilde{T}_0}{T}\right)^{-y} \Phi_2\left[\tilde{\delta}\left(\ln \frac{\tilde{T}_0}{T}\right)^{\frac{1}{\nu\psi}}\right], \quad (5)$$

where both Φ_1 and Φ_2 are unknown function. According to Eq. (5), the temperature dependence of the crossing points can be obtained [9]

$$B_c(T) \approx \tilde{B}_c^* \left[1 - u\left(\ln \frac{\tilde{T}_0}{T}\right)^{-\frac{1}{\nu\psi}-y}\right]. \quad (6)$$

Designating $x_1 = \tilde{\delta}[\ln(\tilde{T}_0/T)]^{1/\nu\psi}$ and $x_2 = [\ln(\tilde{T}_0/T)]^{-y}$, we rewrite Eq. (5) as

$$\tilde{R}(x_1) = R(x_1, T) - x_2(T) \cdot u\Phi_2(x_1), \quad (7)$$

where \tilde{R} is the corrected resistance and R is the measured resistance near B_c . For a certain fixed x_1 , $u\Phi_2(x_1)$ can be obtained from the slope of the $R(x_1, T)$ vs $x_2(T)$, and $\tilde{R}(x_1)$ is then obtained. Thus, one can determine whether the activated scaling is satisfied by checking the \tilde{R} vs $\tilde{\delta}[\ln(\tilde{T}_0/T)]^{1/\nu\psi}$ curve. Experimentally, it has been demonstrated that the low-temperature \tilde{R} data at different temperatures and fields in the vicinity of B_c of the 2D superconductors with QGS follow the prediction of Eq. (5) and collapse onto a single curve [51], which in turn is another hallmark of the emergence of QGS.

To check whether the low-temperature magnetoresistance isotherms of the 3D superconducting MoTiN films deposited at 12.5% $\lesssim P_{N_2} \lesssim 17.5\%$ obey the activated scaling mentioned above, we compare the B_{ci} vs T and low-temperature $\rho(T, B_i)$ data with Eqs. (6) and (5), respectively, where $i = \perp$ and \parallel . Firstly, the theoretical predictions of Eq. (6) are fitted to the B_{ci} vs T data of the films by taking $\nu\psi = 0.60$ [for the $P_{N_2} \simeq 15.0\%$ film in the perpendicular field, see the solid curve in Fig. 5(d) as an example]. Then the fitting parameters B_{ci}^* , \tilde{T}_{0i} , u_i , and y_i can be determined (see Table II). Secondly, fixing $\tilde{\delta}_i[\ln(\tilde{T}_{0i}/T)]^{1/\nu\psi}$ at a certain value, we obtain the value of $u_i\Phi_2$ of the films. Then, the irrelevant correction $\Delta\rho_i = x_2(T) \cdot u_i\Phi_2$ as a function of temperature and the corrected resistivities $\tilde{\rho}_i$ as a function of $\tilde{\delta}_i[\ln(\tilde{T}_{0i}/T)]^{1/\nu\psi}$ for each film are obtained, respectively. As an example, we present the temperature dependence of the irrelevant correction $\Delta\rho_{\perp}$ [$\Delta\rho_{\parallel}$] and the effective resistivity $\tilde{\rho}_{\perp}$ [$\tilde{\rho}_{\parallel}$] variation with the scaling parameter $\tilde{\delta}_{\perp}[\ln(\tilde{T}_{0\perp}/T)]^{1/\nu\psi}$ [$\tilde{\delta}_{\parallel}[\ln(\tilde{T}_{0\parallel}/T)]^{1/\nu\psi}$] for the $P_{N_2} \simeq 15.0\%$ film in the temperature range of 0.50 to 1.10 K [1.20 K] in Figs. 7(a) [Figs. 7(c)] and 7(b) [7(d)], respectively. For this film, $\Delta\rho_{\perp}$ ($\Delta\rho_{\parallel}$) is below 0.235 m Ω cm (0.106 m Ω cm), which is less than 15% (7%) of the resistivity at the field and temperature regimes. In addition, Both $\Delta\rho_{\perp}$ and $\Delta\rho_{\parallel}$

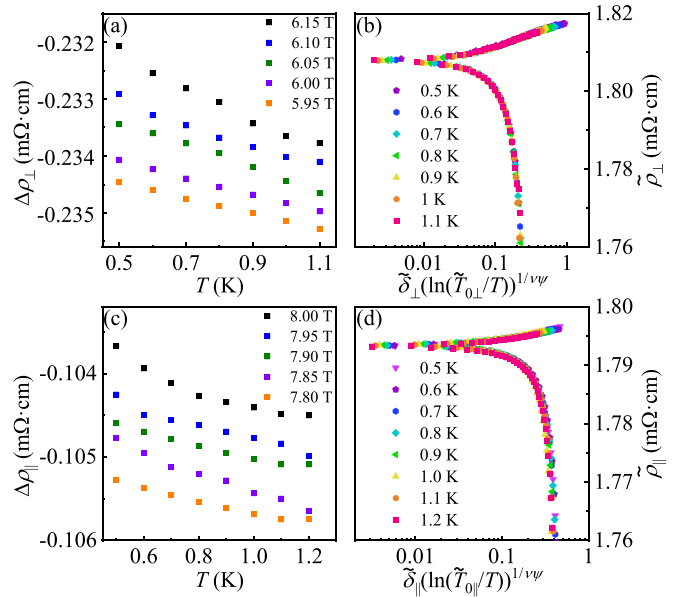


FIG. 7. The activated scaling analysis with the irrelevant correction for the $P_{N_2} \simeq 15.0\%$ film. (a) Temperature dependence of the irrelevant correction at different perpendicular fields. (b) The effective resistivity $\tilde{\rho}_{\perp}$ vs the scaling variable $\tilde{\delta}_{\perp}[\ln(\tilde{T}_{0\perp}/T)]^{1/\nu\psi}$. (c) Temperature dependence of the irrelevant correction at different parallel fields. (d) The effective resistivity $\tilde{\rho}_{\parallel}$ vs the scaling variable $\tilde{\delta}_{\parallel}[\ln(\tilde{T}_{0\parallel}/T)]^{1/\nu\psi}$. Here $\nu\psi$ is taken as 0.60 for both the perpendicular and parallel fields.

decrease with decreasing temperature, being consistent with the theoretical prediction. From Figs. 7(b) and 7(d), one can see that the $\tilde{\rho}_i$ vs $\tilde{\delta}_i[\ln(\tilde{T}_{0i}/T)]^{1/\nu\psi}$ ($i = \perp$ and \parallel) data collapse onto a single curve, satisfying the activated scaling described by Eq. (5). (The corresponding results for the $P_{N_2} \simeq 12.5\%$ and 17.5% films are similar to those for the $P_{N_2} \simeq 15.0\%$ film and given in Fig. S7 within the Supplemental Material [36]). Inspection of Table II indicates the difference between B_{ci}^* [obtained from Eq. (2)] and \tilde{B}_{ci}^* [obtained from Eq. (6)] is less than 3.4% for each film. The results mentioned here confirm the emergence of QGS in these 12.5% $\lesssim P_{N_2} \lesssim 17.5\%$ films.

According to Levellyn *et al.* [9], the value of $\nu\psi$ can also be determined by

$$\frac{1}{\nu z} = \frac{1}{\nu\psi} \frac{1}{\ln(\tilde{T}_0/T)}. \quad (8)$$

As an example, the temperature dependence of $z\nu_{\perp}$ for the $P_{N_2} \simeq 15.0\%$ film is presented in Fig. 8. Taking \tilde{T}_0 as 4.846 (see Table II) and $\nu\psi$ as an adjusting parameter, we fit the $z\nu_{\perp}$ vs T data using Eq. (8), and the result is shown by the solid curve in Fig. 8. Inspection of Fig. 8 indicates that the $z\nu_{\perp}$ vs T data follows the prediction of Eq. (8). The value of the exponent product for the best fit is $\nu\psi \approx 0.63$, which is close to the value $\nu\psi = 0.60$ used in Eqs. (2), (5), and (6). In fact, for all the three films, the values of $\nu\psi$ obtained in fitting Eq. (8) are all closed to 0.60 (the deviations being less than 15%) both in perpendicular and parallel fields. Thus, it is reasonable to take $\nu\psi = 0.60$ in the above analysis using the activated scaling of Eq. (5).

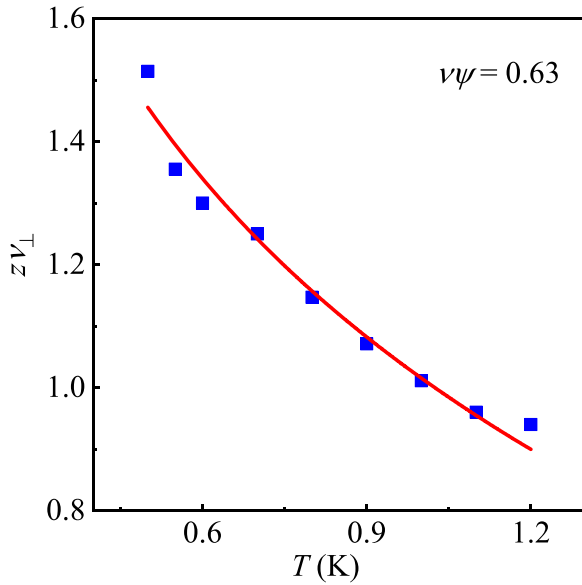


FIG. 8. The temperature dependence of $z\nu_{\perp}$ for the $P_{N_2} \simeq 15.0\%$ film, the solid curve is the least-square fit to Eq. (8).

Theoretically, the QGS in 3D system is stable and originates from the quenched disorder [19–22], which is just like that in 2D system. For the *B1*-type MoN film, it is reported that the fcc structure can be also stable when a lot of vacancies, including both molybdenum and nitrogen vacancies, exist in the fcc conventional cell [29,53]. In the $\text{Mo}_{0.8}\text{Ti}_{0.2}\text{N}_x$ films, x only represents the average atomic ratio of nitrogen to the sum of Mo and Ti and the number of transition metal or nitrogen atoms in each fcc conventional cell is generally less than 4 even if $x \simeq 1$, i.e., there are a lot of Mo (or Ti) and nitrogen vacancies in the *B1*- $\text{Mo}_{0.8}\text{Ti}_{0.2}\text{N}_x$ films. These vacancies are the main source of the quenched disorder. At low temperature and high field (in the vicinity of the critical point of the quantum phase transition), the quenched disorder drives the films into an inhomogeneous superconducting state, in which the superconducting islands or droplets (rare regions) coexist with the disordered bulk of the system. The dynamics of the rare regions is very slow and follows the activated scaling rather than the power-law dynamical scaling. Thus, the sharp transition of the SMT is smeared and QGS then emerges in these $12.5\% \lesssim P_{N_2} \lesssim 17.5\%$ $\text{Mo}_{0.8}\text{Ti}_{0.2}\text{N}_x$ films. For the fcc $(\text{Mo}_{0.8}\text{Ti}_{0.2})_2\text{N}_{1.06}$ film, the low-temperature magnetoresistance isotherms cross at a single point and obey the power-law dynamical scaling. The $k_{\text{F}}\ell$ of the $(\text{Mo}_{0.8}\text{Ti}_{0.2})_2\text{N}_{1.06}$ film is the largest among all the films, which means the disorder strength of this film is the weakest. According to Vojta [54], the effects of quenched disorder on the critical point can be classified into three classes. (1) The average disorder strength decreases with increasing length scale, and the system tends to homogeneous at large length scales. As a result, the influence of the quenched disorder on the critical point becomes unimportant and can be neglected. (2) The system is inhomogeneous at all length scales, but the relative strength of inhomogeneities reaches to a finite value for large length scales. In this system, the critical point still exhibits conventional power-law scaling. However, the critical

exponents become different from those of the clean system. (3) The relative strength of inhomogeneities increases with increasing length scale at any length scale. At these infinite-randomness critical points, the activated scaling instead of the power-law scaling is satisfied. As mentioned above, the fcc Mo_2N is a stable phase [55] while the *B1*-MoN is a metastable phase [56]. Thus, the strength of the inhomogeneities in the fcc $(\text{Mo}_{0.8}\text{Ti}_{0.2})_2\text{N}_{1.06}$ film could be asymptotically unimportant or approach a finite value for large length scale. According to Kuzmiak *et al.* [57], the superconductivity of the fcc Mo_2N is spatially homogeneous, which supports our hypothesis. As a result, the critical point maintains the power-law scaling on the whole.

IV. CONCLUSIONS

A series of ~ 80 -nm-thick epitaxial MoTiN films with NaCl-type structure were grown on (100) MgO single crystal substrates by reactive sputtering method in an Ar and N_2 mixture atmosphere, and their low-temperature electrical transport properties were systematically studied. The composition of the $P_{N_2} \simeq 10.0\%$ film is $(\text{Mo}_{0.8}\text{Ti}_{0.2})_2\text{N}_{1.06}$, while the compositions of the $P_{N_2} \simeq 12.5\%$, $P_{N_2} \simeq 15.0\%$, and $P_{N_2} \simeq 17.5\%$ films are $\text{Mo}_{0.8}\text{Ti}_{0.2}\text{N}_{0.84}$, $\text{Mo}_{0.8}\text{Ti}_{0.2}\text{N}_{1.05}$, and $\text{Mo}_{0.8}\text{Ti}_{0.2}\text{N}_{1.12}$, respectively. All the films reveal superconducting properties at low temperatures and are 3D with respect to superconductivity. A magnetic field, which is either perpendicular or parallel to the film plane, can drive the films transforming from superconducting to bad metallic states. For the $(\text{Mo}_{0.8}\text{Ti}_{0.2})_2\text{N}_{1.06}$ film, the low-temperature magnetoresistance isotherms cross at one single point and the resistivities near the SMT can be described by a power-law scaling deduced from the dirty boson model, which is applicable for both the perpendicular and parallel field. For the $\text{Mo}_{0.8}\text{Ti}_{0.2}\text{N}_x$ ($0.84 \lesssim x \lesssim 1.12$) films, both the critical exponents $z\nu_{\perp}$ and $z\nu_{\parallel}$ diverge in the way same as that for QGS in 2D superconductors when approaching the quantum critical points. In addition, both the perpendicular and parallel corrected resistivities obey an activated scaling based on the random transverse-field Ising model. Our results provide strong experimental evidences for the existence of QGS in 3D superconductors.

ACKNOWLEDGMENTS

The authors are grateful to Prof. Juhn-Jong Lin for valuable discussion. This work is supported by the National Natural Science Foundation of China through Grant No. 12174282.

APPENDIX: CRYSTAL STRUCTURE, ATOMIC VALENCE, AND COMPOSITION

In this Appendix, we provide the crystal structure, atomic valence, and composition information of the MoTiN films. Figure 9(a) shows the XRD θ - 2θ scan patterns of the films deposited at different nitrogen partial pressures and the MgO substrate. In the spectra, the strong peak centered at $\sim 43.02^\circ$ and the weak peaks at $\sim 38.78^\circ$ are the diffractions of MgO (200) plane. The former corresponds to Cu K_{α} radiation, and

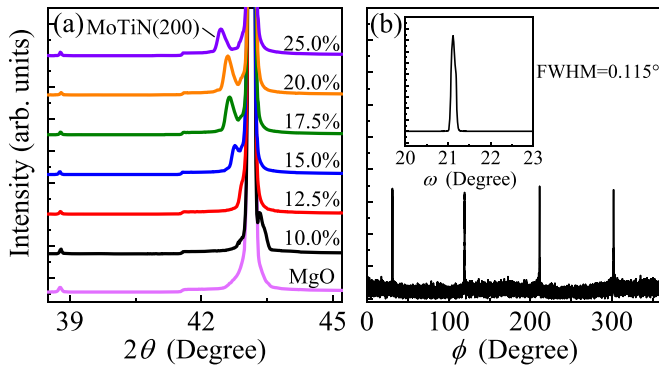


FIG. 9. (a) XRD θ - 2θ scan patterns of MoTiN films deposited at different nitrogen partial pressures. (b) ϕ -scan spectrum of (200) plane for the film deposited at $P_{N_2} \approx 15.0\%$. The inset in (b) is the rocking curve of the (200) diffraction peak of the $P_{N_2} \approx 15.0\%$ film.

the latter is related to Cu K_β radiation. Thus, the lattice constant of the MgO substrate is evaluated to be 4.217 Å. For each film, besides the (200) peaks of the MgO substrate, only the (200) diffraction of the face-centered cubic (fcc) MoTiN can be observed. The values of the lattice constants a can be evaluated using the position of (200) diffractions. For the film deposited at $P_{N_2} \approx 10.0\%$, the value of a is 4.191 Å, which is close to that of γ -Mo₂N [27]. For other films, the values of a increase from 4.228 to 4.272 Å as P_{N_2} increases from 12.5% to 25.0%. These values of the lattice constants are comparable with those of B1-MoN in previous reports [25,26,58]. Since the ionic radius of Ti³⁺ is quite close to that of Mo³⁺ [59], it is deduced that MoTiN films with B1 structure could be formed under 12.5% $\lesssim P_{N_2} \lesssim 25.0\%$. Figure 9(b) shows the ϕ -scan profile of (200) plane of the film deposited at $P_{N_2} \approx 15.0\%$. Four uniformly distributed diffraction peaks can be clearly observed, indicating that the MoTiN film is epitaxially grown on the MgO substrate. The inset of Fig. 9(b) shows the rocking curve of the (200) diffraction peak of the $P_{N_2} \approx 15.0\%$ film. The full width at half maximum (FWHM) of the peak is 0.115°, demonstrating that the film has high crystalline quality. For other films, the ϕ -scan profiles and rocking curves are similar to those of the $P_{N_2} \approx 15.0\%$ film, and the FWHMs of the peaks in the rocking curves are less than 0.12°, which are presented in Fig. S1 within the Supplemental Material [36]. The lattice constant and FWHM of the rocking curve for each film are listed in Table I.

Figure 10 shows the XPS results of the film deposited at $P_{N_2} \approx 10.0\%$, 17.5%, and 25.0% as examples. Among them, Figs. 10(a), 10(b), and 10(c) are the spectra for the $P_{N_2} \approx 10.0\%$ film, Figs. 10(d), 10(e), and 10(f) are the spectra for the $P_{N_2} \approx 17.5\%$ film, and Figs. 10(g), 10(h), and 10(i) are the spectra for the $P_{N_2} \approx 25.0\%$ film. For the Mo 3d spectra, the characteristic peaks can be deconvoluted into two peaks, originating from Mo 3d_{3/2} and Mo 3d_{5/2} of fcc (MoTi)N_x (Mo^{δ+}, 2 < δ < 4), respectively [60,61]. The Ti 2p spectra can also be deconvoluted into two peaks, whose positions are close to those in fcc TiN_x [62]. For the film deposited at $P_{N_2} \approx 17.5\%$, the binding energy of the Mo 3d_{3/2} peak is 231.20 eV, which is nearly identical to that of B1-MoN [28]. As the nitrogen partial pressure is enhanced from 12.5%

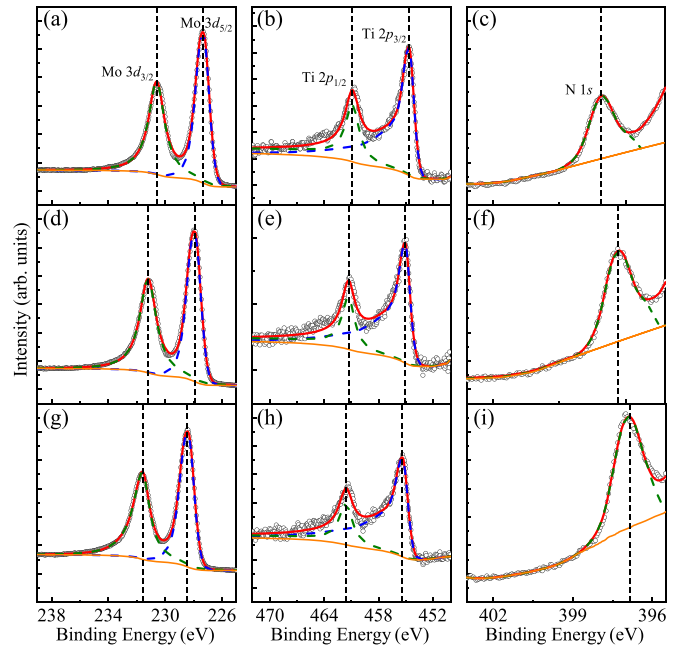


FIG. 10. XPS results of the films deposited at $P_{N_2} \approx 10.0\%$, 17.5%, and 25.0%. (a), (b), and (c) are the spectra of Mo-3d, Ti-2p, and N-1s orbits for the $P_{N_2} \approx 10.0\%$ film. (d), (e), and (f) are the spectra of Mo-3d, Ti-2p, and N-1s orbits for the $P_{N_2} \approx 17.5\%$ film. (g), (h), and (i) are the spectra of Mo-3d, Ti-2p, and N-1s orbits for the $P_{N_2} \approx 25.0\%$ film.

to 25.0%, the binding energies of Mo 3d_{3/2} peaks gradually increase from 230.85 eV to 231.60 eV, which is similar to the results in previous reports [28,61]. The continuous shift of the Mo 3d_{3/2} peaks to the high binding energy can be attributed to the increase of the charge transfer from Mo to N with the increase of the amount of nitrogen atoms in (MoTi)N_x lattice. For the film deposited at $P_{N_2} \approx 10.0\%$, the Mo 3d_{3/2} peak is located at 230.60 eV, which is decreased about 0.25 eV compared with that of the $P_{N_2} \approx 12.5\%$ film. The relative large reduction in binding energy means a great increase of nitrogen vacancies in the $P_{N_2} \approx 10.0\%$ film. The variation trend of the position of Ti 2p_{3/2} peak is similar to that of the Mo 3d_{3/2}, and the position of Ti 2p_{3/2} peak increases from 454.64 eV to 455.35 eV as P_{N_2} is enhanced from 10.0% to 25.0%. As for the N 1s spectra, the binding energy of the peak decreases with increasing P_{N_2} , which is also the result of increasing charge transfer from Mo to N. From the areas of the XPS peaks, one can estimate the atomic ratios of Mo, Ti, and N in the films, and the uncertainties are estimated being less than $\pm 15\%$ [63]. For the films deposited at $P_{N_2} \approx 10.0\%$, 12.5%, 15.0%, 17.5%, 20.0%, and 25.0%, the atomic ratios of Ti to the sum of Mo and Ti are 17.9%, 19.9%, 18.3%, 18.2%, 17.8%, and 18.8%, respectively, i.e., the atomic ratio of Ti to Mo in each film is close to that of the target within experimental uncertainties. The atomic ratio of the metals (Mo and Ti) to nitrogen, denoted by the subscript x in (MoTi)N_x, is also obtained, and listed in Table I. Inspection of Table I indicates that x increases from 0.53 to 1.36 as the nitrogen partial pressure is enhanced from 10.0% to 25.0%. The ratio of metal to nitrogen atoms for the film deposited at $P_{N_2} \approx 10.0\%$ is

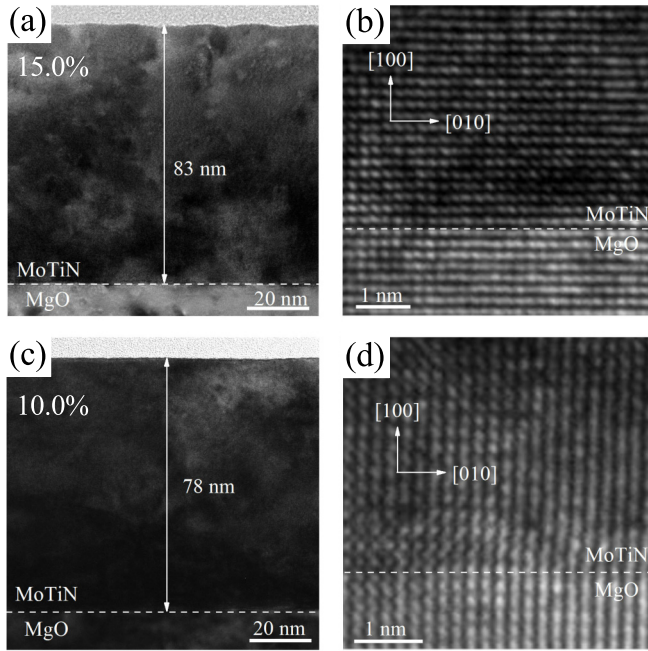


FIG. 11. (a) Cross-sectional HRTEM micrograph of the film deposited at $P_{N_2} \approx 15.0\%$. (b) The enlarged HRTEM image near the MoTiN/MgO interface for (a). (c) Cross-sectional HRTEM micrograph of the film deposited at $P_{N_2} \approx 10.0\%$. (d) The enlarged HRTEM image near the MoTiN/MgO interface for (c).

close to 2 : 1, and that for the film deposited at $P_{N_2} \approx 15.0\%$ is approximately 1 : 1. In the following discussions, the atomic ratio of Mo to Ti is written as 8 : 2 and the atomic ratio of metal to nitrogen is written as x for each film for simplicity. For the molybdenum-nitrogen system, the fcc γ - Mo_2N_y with $0.78 \lesssim y \lesssim 1.08$ is known as a stable phase [55], while $B1$ -MoN is believed to be a metastable phase [56]. The XRD and XPS results discussed above indicate that MoTi-N system can not only form fcc γ - $(\text{Mo}_{0.8}\text{Ti}_{0.2})_2\text{N}$ phase but also be stabilized in $B1$ - $\text{Mo}_{0.8}\text{Ti}_{0.2}\text{N}_x$ phase in a wide range of x . Our results are consistent with those obtained by Sanjinés *et al.* [33].

Figure 11(a) shows the cross-sectional HRTEM micrograph of the $P_{N_2} \approx 15.0\%$ film along the [001] axis. The MoTiN/MgO interface and the surface of the MoTiN film can be clearly identified from the figure. The thickness of the film estimated from the TEM image is ~ 83 nm, which is roughly identical to that obtained by the growth rate and deposition time. Figure 11(b) is the enlarged HRTEM image for a randomly selected area near the MoTiN/MgO interface for the same film. The clear lattice image confirms the epitaxial characteristic of the film. The spacing d between adjacent (100) [or (010)] planes obtained from HRTEM is 0.212 nm, which is consistent with the result obtained from XRD. The cross-sectional HRTEM images for the $P_{N_2} \approx 12.5\%$ and 17.5% films are similar to that for the $P_{N_2} \approx 15.0\%$ one, and are presented in Fig. S2 within the Supplemental Material [36]. Figures 11(c) and 11(d) show the cross-sectional HRTEM micrograph along the [001] axis and the enlarged HRTEM image near the MoTiN/MgO interface for the $P_{N_2} \approx 10.0\%$ film. The thickness of the film is ~ 78 nm, which is close to the expected 80 nm. Compared with the $P_{N_2} \approx 15.0\%$ film, the $P_{N_2} \approx 10.0\%$ film have more defects, including atomic vacancies and slight lattice distortion near the MoTiN/MgO interface. Since the ratio of metal to nitrogen atoms seriously deviates from 1 : 1 for the $(\text{Mo}_{0.8}\text{Ti}_{0.2})_2\text{N}_{1.06}$ film with NaCl structure, there are more nitrogen vacancies in the $P_{N_2} \approx 10.0\%$ film compared with the others, which is what we observed in the cross-sectional HRTEM images. The interspace distance of the (010) planes is 0.211 nm near the MoTiN/MgO interface, being slightly larger than that (0.210 nm) of the (100) planes [the interspace distance of the (100) planes is 0.210 nm, which is almost identical to that obtained from the out-plane XRD measurement]. When the distance to the interface is greater than ~ 1 nm, interspace distance of the (010) planes returns to 0.210 nm. Thus, the extension of d for the (100) planes is caused by the mismatch of lattices between the $(\text{Mo}_{0.8}\text{Ti}_{0.2})_2\text{N}_{1.06}$ film and the MgO substrate. The TEM results support the conclusion that the film deposited at $P_{N_2} \approx 10.0\%$ crystallizes into a γ - $(\text{Mo}_{0.8}\text{Ti}_{0.2})_2\text{N}$ phase and the films deposited at $12.5\% \lesssim P_{N_2} \lesssim 17.5\%$ are stabilized to a $B1$ -type $\text{Mo}_{0.8}\text{Ti}_{0.2}\text{N}_x$ phase.

- [1] Y. Xing, H. M. Zhang, H. L. Fu, H. Liu, Y. Sun, J. P. Peng, F. Wang, X. Lin, X. C. Ma, Q. K. Xue *et al.*, Quantum Griffiths singularity of superconductor-metal transition in Ga thin films, *Science* **350**, 542 (2015).
- [2] S. C. Shen, Y. Xing, P. J. Wang, H. W. Liu, H. L. Fu, Y. W. Zhang, L. He, X. C. Xie, X. Lin, J. C. Nie, and J. Wang, Observation of quantum Griffiths singularity and ferromagnetism at the superconducting $\text{LaAlO}_3/\text{SrTiO}_3(110)$ interface, *Phys. Rev. B* **94**, 144517 (2016).
- [3] Y. Xing, K. Zhao, P. Shan, F. Zheng, Y. Zhang, H. Fu, Y. Liu, M. Tian, C. Xi, H. Liu *et al.*, Ising superconductivity and quantum phase transition in macro-size monolayer NbSe_2 , *Nano Lett.* **17**, 6802 (2017).
- [4] Y. Saito, T. Nojima, and Y. Iwasa, Quantum phase transitions in highly crystalline two-dimensional superconductors, *Nat. Commun.* **9**, 778 (2018).
- [5] M. C. de Andrade, R. Chau, R. P. Dickey, N. R. Dilley, E. J. Freeman, D. A. Gajewski, M. B. Maple, R. Movshovich, A. H. Castro Neto, G. Castilla, and B. A. Jones, Evidence for a common physical description of non-Fermi-liquid behavior in chemically substituted f-electron systems, *Phys. Rev. Lett.* **81**, 5620 (1998).
- [6] A. H. Castro Neto, G. Castilla, and B. A. Jones, Non-Fermi liquid behavior and Griffiths phase in f-electron compounds, *Phys. Rev. Lett.* **81**, 3531 (1998).
- [7] A. Steppke, R. Kuchler, S. Lausberg, E. Lengyel, L. Steinke, R. Borth, T. Lühmann, C. Krellner, M. Nicklas, C. Geibel *et al.*, Ferromagnetic quantum critical point in the heavy-fermion metal $\text{YbNi}_4(\text{P}_{1-x}\text{As}_x)_2$, *Science* **339**, 933 (2013).
- [8] S. Ubaid-Kassis, T. Vojta, and A. Schroeder, Quantum Griffiths phase in the weak itinerant ferromagnetic alloy $\text{Ni}_{1-x}\text{V}_x$, *Phys. Rev. Lett.* **104**, 066402 (2010).

- [9] N. A. Lewellyn, I. M. Percher, J. Nelson, J. Garcia-Barriocanal, I. Volotsenko, A. Frydman, T. Vojta, and A. M. Goldman, Infinite-randomness fixed point of the quantum superconductor-metal transitions in amorphous thin films, *Phys. Rev. B* **99**, 054515 (2019).
- [10] X. Zhang, A. E. Lita, H. Liu, V. B. Verma, Q. Zhou, S. W. Nam, and A. Schilling, Size dependent nature of the magnetic-field driven superconductor-to-insulator quantum-phase transitions, *Commun. Phys.* **4**, 100 (2021).
- [11] C. Huang, E. Zhang, Y. Zhang, J. Zhang, F. Xiu, H. Liu, X. Xie, L. Ai, Y. Yang, M. Zhao *et al.*, Observation of thickness-tuned universality class in superconducting β -W thin films, *Sci. Bull.* **66**, 1830 (2021).
- [12] I. A. Verzhbitskiy, D. Voiry, M. Chowalla, and G. Eda, Disorder-driven two-dimensional quantum phase transitions in Li_xMoS_2 , *2D Mater.* **7**, 035013 (2020).
- [13] T. Jing, Z. Han, Z. He, M. Shao, P. Li, and Z. Li, Quantum phase transition in NbN superconducting thin films, *Phys. Rev. B* **107**, 184515 (2023).
- [14] X. Wang, L. Wang, Y. Liu, F. Chen, W. Gao, Y. Wu, Z. Xu, W. Peng, Z. Wang, Z. Di, W. Li, G. Mu, and Z. Lin, Robust quantum Griffiths singularity above 1.5 K in nitride thin films, *Phys. Rev. B* **107**, 094509 (2023).
- [15] Y. Liu, S. Qi, J. Fang, J. Sun, C. Liu, Y. Liu, J. Qi, Y. Xing, H. Liu, X. Lin, L. Wang, Q. Xue, X. Xie, and J. Wang, Observation of in-plane quantum Griffiths singularity in two-dimensional crystalline superconductors, *Phys. Rev. Lett.* **127**, 137001 (2021).
- [16] R. B. Griffiths, Nonanalytic behavior above the critical point in a random Ising ferromagnet, *Phys. Rev. Lett.* **23**, 17 (1969).
- [17] C. Pich, A. P. Young, H. Rieger, and N. Kawashima, Critical behavior and Griffiths-McCoy singularities in the two-dimensional random quantum Ising ferromagnet, *Phys. Rev. Lett.* **81**, 5916 (1998).
- [18] I. A. Kovács and F. Iglói, Renormalization group study of the two-dimensional random transverse-field Ising model, *Phys. Rev. B* **82**, 054437 (2010).
- [19] O. Motrunich, S. Mau, D. A. Huse, and D. S. Fisher, Infinite-randomness quantum Ising critical fixed points, *Phys. Rev. B* **61**, 1160 (2000).
- [20] T. Vojta, A. Farquhar, and J. Mast, Infinite-randomness critical point in the two-dimensional disordered contact process, *Phys. Rev. E* **79**, 011111 (2009).
- [21] A. Del Maestro, B. Rosenow, J. A. Hoyos, and T. Vojta, Dynamical conductivity at the dirty superconductor-metal quantum phase transition, *Phys. Rev. Lett.* **105**, 145702 (2010).
- [22] B. Fan and A. M. García-García, Superconductivity at the three-dimensional Anderson metal-insulator transition, *Phys. Rev. B* **102**, 184507 (2020).
- [23] We recently found a preprint, in which the QGS was also observed in a spinel oxide MgTi_2O_4 , was announced in arXiv (see Ref. [24]).
- [24] S. Qi, Y. Liu, Z. Wang, F. Chen, Q. Li, H. Ji, R. Li, Y. Li, J. Fang, H. Liu *et al.*, Quantum Griffiths singularity in three-dimensional superconductor to Anderson critical insulator transition, arXiv:2311.06710.
- [25] W. E. Pickett, B. M. Klein, and D. A. Papaconstantopoulos, Theoretical prediction of MoN as a high T_c superconductor, *Physica B+C* **107**, 667 (1981).
- [26] Y. Zhao and S. He, B1-type MoN, a possible high T_c superconductor, *Solid State Commun.* **45**, 281 (1983).
- [27] H. Ihara, Y. Kimura, K. Senzaki, H. Kezuka, and M. Hirabayashi, Electronic structures of B1 MoN, fcc Mo_2N , and hexagonal MoN, *Phys. Rev. B* **31**, 3177 (1985).
- [28] K. Inumaru, K. Baba, and S. Yamanaka, Structural distortion and suppression of superconductivity in stoichiometric B1-MoN epitaxial thin films, *Phys. Rev. B* **73**, 052504 (2006).
- [29] B. D. Ozsdolay, K. Balasubramanian, and D. Gall, Cation and anion vacancies in cubic molybdenum nitride, *J. Alloys Compd.* **705**, 631 (2017).
- [30] D. A. Papaconstantopoulos and W. E. Pickett, Effects of disorder on high-temperature superconductivity in cubic MoN, *Phys. Rev. B* **31**, 7093 (1985).
- [31] Y. H. Shi, B. R. Zhao, Y. Y. Zhao, L. Li, and J. R. Liu, Superconducting and normal-state properties of MoN_x thin films, *Phys. Rev. B* **38**, 4488 (1988).
- [32] G. L. W. Hart and B. M. Klein, Phonon and elastic instabilities in MoC and MoN, *Phys. Rev. B* **61**, 3151 (2000).
- [33] R. Sanjinés, C. Wiemer, J. Almeida, and F. Lévy, Valence band photoemission study of the Ti-Mo-N system, *Thin Solid Films* **290-291**, 334 (1996).
- [34] A. F. Ioffe and A. R. Regel, Non-crystalline, amorphous, and liquid electronic semiconductors, in *Progress in Semiconductors* edited by A. F. Gibson, F. A. Kroger, and R. E. Burgess (Heywood, London, 1960), Vol. 4, pp. 237–291.
- [35] M. Tinkham, *Introduction to Superconductivity*, 2nd ed (Dover Publications, Mineola, NY, 1996).
- [36] See Supplemental Material at <http://link.aps.org/supplemental/10.1103/PhysRevB.109.224508> for the XRD results and the resistivity vs temperature data at different magnetic fields of the $P_{\text{N}_2} \simeq 10.0\%$, 12.5% , and 17.5% films. The TEM results and the behaviors of the low-temperature magnetoresistance isotherms of the $P_{\text{N}_2} \simeq 12.5\%$ and 17.5% films are also included in the Supplemental Material.
- [37] A. Yazdani and A. Kapitulnik, Superconducting-insulating transition in two-dimensional α -MoGe thin films, *Phys. Rev. Lett.* **74**, 3037 (1995).
- [38] M. A. Steiner, N. P. Breznay, and A. Kapitulnik, Approach to a superconductor-to-Bose-insulator transition in disordered films, *Phys. Rev. B* **77**, 212501 (2008).
- [39] N. P. Breznay, M. A. Steiner, S. A. Kivelson, and A. Kapitulnik, Self-duality and a Hall-insulator phase near the superconductor-to-insulator transition in indium-oxide films, *Proc. Natl. Acad. Sci. USA* **113**, 280 (2016).
- [40] M. P. A. Fisher, P. B. Weichman, G. Grinstein, and D. S. Fisher, Boson localization and the superfluid-insulator transition, *Phys. Rev. B* **40**, 546 (1989).
- [41] M. P. A. Fisher, Quantum phase transitions in disordered two-dimensional superconductors, *Phys. Rev. Lett.* **65**, 923 (1990).
- [42] Z. Wang, Y. Liu, C. Ji, and J. Wang, Quantum phase transitions in two-dimensional superconductors: A review on recent experimental progress, *Rep. Prog. Phys.* **87**, 014502 (2024).
- [43] A. Rogachev and B. Sacépé, Deficiency of the scaling collapse as an indicator of a superconductor-insulator quantum phase transition, *Phys. Rev. B* **101**, 235164 (2020).
- [44] A. M. Goldman and N. Marković, Superconductor-insulator transitions in the two-dimensional limit, *Phys. Today* **51**(11), 39 (1998).

- [45] S. L. Sondhi, S. M. Girvin, J. P. Carini, and D. Shahar, Continuous quantum phase transitions, *Rev. Mod. Phys.* **69**, 315 (1997).
- [46] A. M. Goldman, Superconductor-insulator transitions, *Int. J. Mod. Phys. B* **24**, 4081 (2010).
- [47] H. Aubin, C. A. Marrache-Kikuchi, A. Pourret, K. Behnia, L. Bergé, L. Dumoulin, and J. Lesueur, Magnetic-field-induced quantum superconductor-insulator transition in $\text{Nb}_{0.15}\text{Si}_{0.85}$, *Phys. Rev. B* **73**, 094521 (2006).
- [48] N. Mason and A. Kapitulnik, Dissipation effects on the superconductor-insulator transition in 2D superconductors, *Phys. Rev. Lett.* **82**, 5341 (1999).
- [49] P. Giraldo-Gallo, H. Lee, Y. Zhang, M. J. Kramer, M. R. Beasley, T. H. Geballe, and I. R. Fisher, Field-tuned superconductor-insulator transition in $\text{BaPb}_{1-x}\text{Bi}_x\text{O}_3$, *Phys. Rev. B* **85**, 174503 (2012).
- [50] A. B. Harris, Effect of random defects on the critical behaviour of Ising models, *J. Phys. C: Solid State Phys.* **7**, 1671 (1974).
- [51] Z. Cui, L. Pan, J. Fang, S. Qi, Y. Xing, H. Liu, Y. Liu, and J. Wang, The activated scaling behavior of quantum Griffiths singularity in two-dimensional superconductors, *J. Phys. D: Appl. Phys.* **56**, 374002 (2023).
- [52] We use \tilde{B}_c^* here to distinguish the characteristic field B_c^* in Eq. (2).
- [53] Y. Xiao, Z. Han, G. Zhang, and Y. Liang, Understanding the role of atomic vacancies in the stability and hardening of cubic tungsten and molybdenum nitrides, *J. Phys. Chem. C* **127**, 22984 (2023).
- [54] T. Vojta, Rare region effects at classical, quantum and nonequilibrium phase transitions, *J. Phys. A: Math. Gen.* **39**, R143 (2006).
- [55] M. B. Kanoun, S. Goumri-Said, and M. Jaouen, Structure and mechanical stability of molybdenum nitrides: A first-principles study, *Phys. Rev. B* **76**, 134109 (2007).
- [56] H. Jehn, P. Ettmayer, The molybdenum-nitrogen phase diagram, *J. Less-Common Met.* **58**, 85 (1978).
- [57] M. Kuzmiak, M. Kopčík, F. Košuth, V. Vaňo, J. Haniš, T. Samuely, V. Latyshev, O. Onufrienko, V. Komanický, J. Kačmarčík, M. Žemlička, M. Gmitra, P. Szabó, and P. Samuely, Disorder- and magnetic field-tuned fermionic superconductor-insulator transition in MoN thin films: Transport and scanning tunneling microscopy, *Phys. Rev. B* **108**, 184511 (2023).
- [58] G. Linker, R. Smithey, and O. Meyer, Superconductivity in MoN films with NaCl structure, *J. Phys. F: Met. Phys.* **14**, L115 (1984).
- [59] R. D. Shannon, Revised effective ionic radii and systematic studies of interatomic distances in halides and chalcogenides, *Acta Cryst. A* **32**, 751 (1976).
- [60] G. Kim, T. Park, H. Chung, Y. Kim, M. Kwon, and J. Choi, Growth and characterization of chloronitroaniline crystals for optical parametric oscillators: I. XPS study of Mo-based compounds, *Appl. Surf. Sci.* **152**, 35 (1999).
- [61] Y. Wang and R. Y. Lin, Amorphous molybdenum nitride thin films prepared by reactive sputter deposition, *Mater. Sci. Eng. B* **112**, 42 (2004).
- [62] M. Delfino, J. A. Fair, and D. Hodul, X-ray photoemission spectra of reactively sputtered TiN, *J. Appl. Phys.* **71**, 6079 (1992).
- [63] D. Briggs and M. P. Seah, *Practical Surface Analysis by Auger and X-ray Photoelectron Spectroscopy* (John Wiley, New York, 1983).